energies

MDPI

Article

Transient Thermal Behavior and Thermal Buffering of a Novel PCM-Integrated Cavity Solar Receiver

Gülden Adıyaman [1,*] and Levent Çolak [2]

[1] Quality Control in Production Program, Department of Machinery and Metal Technologies, Anatolia Organized Industrial Zone Vocational School, Başkent University, 06909 Ankara, Türkiye
[2] Mechanical Engineering Department, Faculty of Engineering, Başkent University, 06790 Ankara, Türkiye; lcolak@baskent.edu.tr
* Correspondence: gulden@baskent.edu.tr

Abstract

Parabolic trough solar collectors are promising technologies for supplying thermal energy; however, their performance is strongly dependent on the continuity of solar irradiation. Solar interruptions can cause rapid reductions in heat transfer fluid (HTF) temperatures and reduce thermal stability and performance. This study numerically investigates the thermal behavior of a novel phase-change material (PCM)-integrated cavity receiver, patented under Turkish Patent No. 2021/013862, developed to reduce temperature fluctuations during solar interruptions. The receiver combines a cavity configuration with a PCM-based latent heat storage layer. A three-dimensional transient CFD model using the enthalpy–porosity approach was used to simulate melting and solidification. High-density polyethylene (HDPE) was employed as the PCM, while water was used as the HTF. Under the investigated solar irradiation condition, the novel solar receiver absorbed 2458 W. The water outlet temperature reached 437.52 K when the HDPE completely melted at approximately 31 min. During charging, the HDPE stored 2021.4 kJ of thermal energy, comprising both sensible and latent heat. Sensible heat accounted for 55.8% of the total energy stored in the HDPE, while latent heat accounted for 44.2%. Following solar interruption, solidification was completed at approximately 21 min. During solidification, the water outlet temperature decrease was 17.5 K for the PCM-integrated receiver, compared with 58 K for the non-PCM receiver, representing a 69.8% reduction in temperature decrease. The water outlet temperature decrease in the PCM-integrated receiver corresponded to only 4.3% during the solidification period when direct radiation was interrupted. The results demonstrate that the proposed receiver provides effective thermal buffering and improves thermal stability under short-term solar interruption.

Keywords: phase change material; cavity solar receiver; parabolic trough collector; thermal energy storage; solar irradiation interruption; transient CFD; HDPE; latent heat storage

Check for updates

Academic Editor: Stéphane Grieu

Received: 25 September 2026
Revised: 16 October 2026
Accepted: 22 October 2026
Published: 27 October 2026

Copyright: © 2026 by the authors. Licensee MDPI, Basel, Switzerland. This article is an open access article distributed under the terms and conditions of the Creative Commons Attribution (CC BY) license.

1. Introduction

Parabolic trough collectors (PTCs) constitute a commercially well-established class of concentrating solar thermal technologies for converting solar radiation into thermal energy. Their performance is strongly influenced by the optical characteristics of the collector–receiver system, the absorbed solar radiation, and the heat transfer occurring at the receiver–heat transfer fluid (HTF) interface. However, the intermittent nature of solar radiation, caused by cloud passages and atmospheric conditions, can cause fluctuations in HTF temperatures and consequently affect system stability. Thermal energy storage (TES) is

therefore an important application for improving the operational stability of concentrating solar thermal systems [1–3].

Among TES technologies, latent heat thermal energy storage using phase-change materials (PCMs) has attracted considerable attention because it has high energy storage capacity and the ability to store and release heat within a relatively narrow temperature range [1,2]. Integrating PCM directly into solar collectors and receivers is particularly attractive because thermal energy can be stored close to the solar absorption area. Guerraiche et al. [4] investigated a PCM-integrated parabolic trough solar collector. They demonstrated the thermal compensating effect of PCM during short-term cloudy conditions and showed that the system had higher outlet water temperatures than the conventional configuration. Senthil and Cheralathan [5] similarly showed that PCM integration of a concentrated solar receiver provided a thermal buffering effect and increased the thermal energy storage capacity.

Recent studies have continued to investigate PCM integration as a means of mitigating the effects of intermittent solar energy input. Reviews of PCM-based solar thermal storage have emphasized that the melting temperature, latent heat capacity, thermal conductivity, and phase stability of the storage material must be matched to the operating conditions of the application [6]. These factors are particularly relevant to medium-temperature solar receivers, where the PCM transition temperature must be compatible with the receiver temperature and the HTF operating range.

The thermal performance of PCM-integrated receivers depends on the PCM arrangement and operating conditions. Bashir and Giovannelli [7] numerically investigated a PCM-integrated solar receiver and showed that receiver geometry, PCM properties, incident solar flux, and HTF operating conditions affected the thermal behavior and storage performance of the receiver. Senthil [8] experimentally examined the charging behavior of PCMs within vertical and horizontal rectangular enclosures employed for a solar receiver and found that the enclosure placement affected the melting behavior and temperature distribution. These studies demonstrate that PCM performance is closely related to the receiver configuration and heat transfer conditions.

Mohammed et al. [9] developed a transient thermo-optical and phase-change model for a parabolic trough collector integrated with nano-enhanced PCM, combining optical and thermal analyses with the simulation of melting and solidification. Their work addresses the coupled nature of optical loading and PCM thermal behavior. In a separate study, a tube-bundle cavity receiver for a PTC was investigated using three-dimensional CFD [10], highlighting the importance of receiver configuration in determining temperature distribution and thermal performance. This provides complementary evidence that receiver geometry must be considered when evaluating thermal behavior under concentrated solar irradiation.

PCM integration in solar collector configurations has also been investigated in recent years. Chopra et al. [11] experimentally evaluated a PCM-integrated manifold for evacuated tube for use in solar collectors and demonstrated the feasibility of storing thermal energy directly within the collector system. Chopra et al. [12] compared PCM-integrated and conventional evacuated tube collectors and reported that PCM integration improved thermal performance and stability for the collector system. They demonstrate the potential of integrating latent heat storage directly into solar thermal collectors.

Chakraborty [13] numerically investigated the use of fins and PCM in PTCs to improve heat transfer. Anand and Kumar [14] examined the thermal performance of parabolic trough collectors using different HTFs and a thermal storage system, considering the effects of storage materials and operating conditions. A hybrid sand–PCM storage configuration driven by a PTC has also been investigated in terms of charging and discharging performance [15]. These studies indicate that storage material properties, receiver configuration,

and heat transfer enhancement techniques can all influence the transient thermal response of solar thermal systems.

In addition to solar-specific applications, recent work has examined how PCM arrangement and heat transfer enhancement techniques affect melting behavior in latent heat storage systems. Hanchi et al. [16] numerically investigated a finned triplex-tube thermal energy storage system incorporating cascaded PCMs with different melting temperatures. They reported that the order in which the PCMs were arranged and the incorporation of fins strongly affected the melting duration. This demonstrates the importance of PCM configuration and heat-transfer characteristics in determining transient phase-change behavior.

More recent studies have focused on the behavior of PCM-integrated receivers under variable or interrupted solar irradiation. Bashir and Ali [17] investigated a PCM-integrated solar receiver with a double helical tube configuration and considered both melting and solidification under solar flux interruption. They found that the tube arrangement affected the temperature distribution, melting and solidification rates, and fluid outlet temperature. Bagherzadeh et al. [18] experimentally investigated cascaded latent heat storage in a PTC and showed that the PCM configuration and HTF flow rate affected the melting behavior and energy storage capability. Alturki et al. [19] investigated a PTC with a PCM-integrated flat metallic receiver and reported improved temperature stability and thermal performance under variable solar flux.

The transient response of PCM-based solar thermal systems has also been addressed in recent coupled modeling studies. Lim and Sobhansarbandi [20] presented a transient modeling approach for a solar thermal collector incorporating energy storage, combining optical and thermal modeling to evaluate system behavior. A multi-chamber PCM-integrated absorber tube has also been investigated numerically for solar parabolic trough desalination applications, with particular attention to stored-heat utilization during periods without direct solar input [21]. These studies reinforce the importance of evaluating not only the charging process under solar irradiation but also the thermal behavior after the solar input is reduced or interrupted. However, the behavior remains dependent on the receiver geometry, PCM arrangement, and operating conditions considered.

Cavity receivers have also been investigated as an effective approach for improving the utilization of concentrated solar radiation. Multiple reflections within the cavity can enhance radiation absorption. However, cavity performance is strongly affected by geometry, aperture dimensions, and receiver position. Wasankar and Gulhane [22] reviewed different solar cavity receivers and showed the importance of cavity geometry and aperture size in terms of heat loss characteristics. Therefore, the integration of PCM with cavity receivers can enable the effective utilization of radiation and latent heat storage. Nandanwar and Walke [23] investigated a PCM-integrated cavity receiver and demonstrated its thermal buffering potential during periods of reduced solar irradiation. Saravanan et al. [24] similarly investigated a cavity receiver with PCM and showed that PCM integration could improve thermal performance and exergetic efficiency under different conditions.

Research on cavity and receiver thermal design has further highlighted the need to account for the distribution of concentrated solar radiation. Numerical investigations of cavity and tubular receivers have examined the effect of geometry and non-uniform heat flux on temperature distribution and the thermal performance [10,25]. They support the need to investigate the interaction between optical loading, receiver geometry, and transient thermal behavior rather than treating these aspects independently.

Recent reviews and system-level investigations have likewise emphasized the importance of selecting storage materials and operating conditions that provide a suitable balance between heat storage capacity, heat transfer rate, and thermal stability [6,26]. However, findings obtained from hybrid solar systems or from storage units with different geometries

cannot be directly transferred to the receiver without accounting for differences in thermal boundary conditions, PCM properties, and operating temperatures.

Selecting the PCM is another important design consideration. Its phase-change temperature should be compatible with the receiver's operating temperature, and its latent heat and other thermophysical properties affect the storage performance [1,2,27]. High-density polyethylene (HDPE) is a promising polymeric PCM for medium-temperature thermal energy storage. Zauner et al. [28] experimentally investigated HDPE for heat storage and showed it was suitable and had stability over repeated heating and cooling cycles. Weingrill et al. [29] investigated the long-term thermo-oxidative stability of HDPE. They reported only a small reduction in storage capacity after prolonged exposure in the molten phase.

The receiver investigated in the present study was developed based on a novel cavity receiver concept proposed in our previous study [30]. In that study, different cavity geometries, aperture dimensions, and receiver positions were investigated using optical analysis and optimized using response surface methodology. The optimum configuration was determined based on the maximum absorbed solar radiation and established the optical design of the receiver cavity considered herein. Thus, the present study focuses on the transient thermal behavior and latent heat storage performance of the developed receiver.

Accordingly, this study aims to numerically examine the transient thermal behavior of a novel PCM-integrated, self-insulated cavity receiver for a PTC. A three-dimensional CFD model is employed to evaluate the coupled thermal response of the HTF and PCM during melting, complete charging, solar irradiation interruption, and solidification. The thermal behavior of the proposed receiver is also compared with that of an equivalent cavity receiver without PCM under the same operating conditions. The originality and novelty of the study lie in the combined evaluation of the patented cavity receiver, a realistic non-uniform concentrated solar radiation distribution, HDPE-based latent heat storage, and the complete charging–solar interruption–solidification process. The results demonstrate the ability of the proposed receiver to reduce HTF temperature fluctuations. In particular, the study highlights the thermal buffering capability of the proposed receiver during temporary interruptions in direct solar irradiation.

2. Methodology

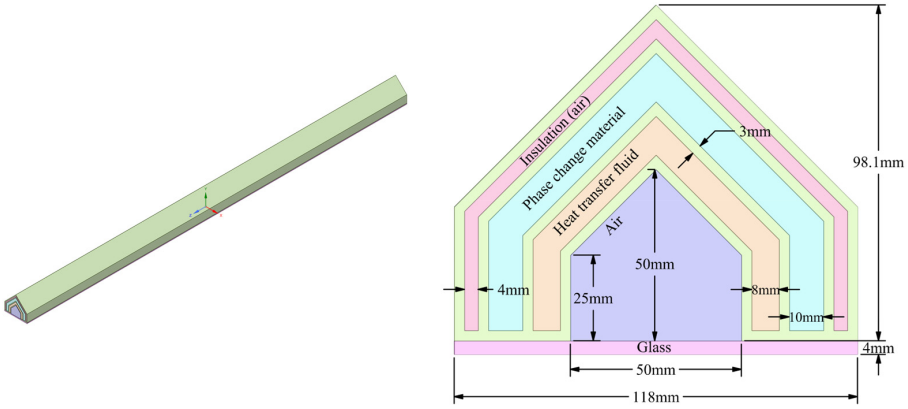
2.1. The Solar Receiver Concept

The receiver concept investigated in this study is a novel cavity-based configuration combining a phase-change material (PCM) and a self-insulated area, and is protected by Turkish Patent No. 2021/013862. The concept was developed to reduce problems, including optical losses, thermal losses to the surroundings, and rapid temperature variations during interruptions in solar irradiation. The cavity configuration enhances the use of concentrated solar radiation, while the insulation layer limits heat losses from the receiver. The integrated PCM provides thermal energy storage for thermal buffering, and this behavior helps to maintain the HTF temperature and prevents the sudden temperature decrease when direct solar irradiation is interrupted.

The cavity geometry used in the present study was based on the optimum configuration determined in our previous optical optimization study [30]. In that study, a polygonal cavity with a width and height of 50 mm and a receiver position at the focal line of the parabolic trough collector was identified as the optimum configuration [30]. Based on this configuration, a three-dimensional receiver with a total length of 2 m was developed using Ansys SpaceClaim v23 R2.

The receiver consists of an 8 mm thick heat transfer fluid (HTF) channel, with water used as the HTF in the present study, a 10 mm thick PCM layer, a 4 mm thick outer air layer used as insulation, and 3 mm thick aluminum walls. A 4 mm thick low-iron glass plate

closes the lower part of the cavity. The glass is used to reduce heat losses from the cavity to the surroundings. It transmits short-wave solar radiation while blocking the transmission of long-wave radiation emitted from the receiver's inner surfaces. Figure 1 presents the resulting layered configuration and dimensions of the receiver.



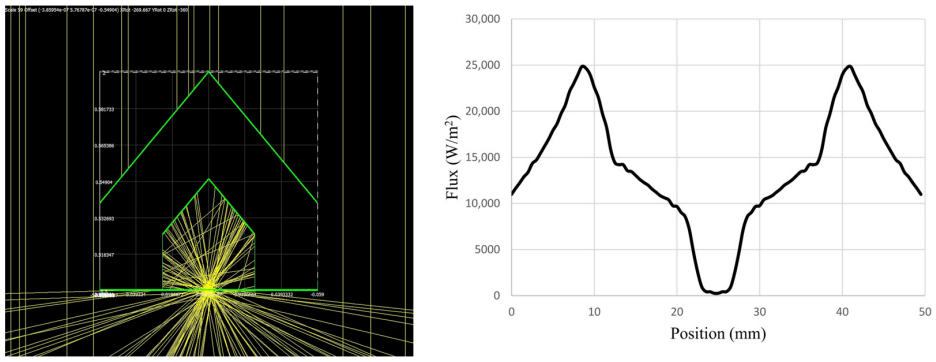
(**a**) (**b**)

Figure 1. Physical configuration of the PCM-integrated, self-insulated cavity receiver: (**a**) three-dimensional model; (**b**) front view with principal dimensions and layers.

2.2. Optical Model and Solar Radiation Mapping

The optical model was previously validated using the LS-2 parabolic trough collector experimentally tested at Sandia [30]. The heat flux distribution obtained from SolTrace exhibited a trend consistent with the literature results and showed close agreement in the maximum and minimum values. This comparison further supported the reliability of the optical model [30]. For the maximum heat flux value, SolTrace was 52,443.76 W/m^2, compared with 48,618 W/m^2 and 52,878 W/m^2 reported by Hachicha et al. [31] and He et al. [32], respectively, corresponding to relative errors of 7.87% and 0.82%, respectively.

The optical analysis of the final novel receiver configuration was performed using SolTrace to determine the absorbed solar radiation and its distribution over the inner cavity surfaces. The analysis was conducted under the meteorological conditions recorded on 18 July 2023 in Etimesgut, Ankara, with a direct solar irradiation of 789 W/m^2. The total solar radiation absorbed by the receiver was calculated as 2458 W. The absorbed radiation was non-uniformly distributed over the cavity surfaces, with approximately 720 W on each of the left and right vertical surfaces and 509 W on each of the upper surfaces. The optical analysis and the resulting radiation distribution over the cavity surfaces are given in Figure 2.



(**a**) (**b**)

Figure 2. Optical analysis and solar radiation map of the proposed PCM-integrated cavity receiver. (**a**) View of the receiver in optical analysis. (**b**) Radiation map over the inner cavity walls.

2.3. Mathematical Model

The thermal and flow behavior of the proposed receiver was simulated in Ansys Fluent using the finite-volume approach. The three-dimensional simulations were performed using the k-ε turbulence model. The conservation equations for mass, momentum, and energy were solved throughout the computational domain. The PCM melting and solidification processes were incorporated into the thermal model. The governing equations were formulated based on conservation [33].

The continuity equation is

$$\frac{\partial(\rho)}{\partial t} + \frac{\partial}{\partial x_i}(\rho u_i) = 0 \tag{1}$$

The momentum equation is expressed as

$$\frac{\partial(\rho u_i)}{\partial t} + \frac{\partial}{\partial x_j}\left(\rho u_i u_j\right) = -\frac{\partial p}{\partial x_i} + \frac{\partial}{\partial x_j}\left[\mu\left(\frac{\partial u_i}{\partial x_j} + \frac{\partial u_j}{\partial x_i} - \frac{2}{3}\delta_{ij}\frac{\partial u_i}{\partial x_i}\right)\right] + \frac{\partial}{\partial x_j}\left(-\rho\overline{u_i' u_j'}\right) \tag{2}$$

where ρ and μ are the fluid density and dynamic viscosity, respectively. u_i and u_j are velocity components; x_i, x_j are spatial coordinates; t is time; and the thermodynamic pressure is p. The term in the equation $\overline{u_i' u_j'}$ represents Reynolds-stress components. The energy equation is written as

$$\frac{\partial(\rho E)}{\partial t} + \frac{\partial}{\partial x_i}[u_i(\rho E + p)] = \frac{\partial}{\partial x_j}\left[\gamma_{eff}\frac{\partial T}{\partial x_j} + u_i\left(\tau_{ij}\right)_{eff}\right] + W_h \tag{3}$$

where T is the temperature, E is the total energy, W_h is the energy source term, and γ_{eff} is the effective thermal conductivity, defined as

$$\gamma_{eff} = \gamma + \gamma_t \tag{4}$$

The turbulent thermal conductivity is calculated from

$$\gamma_t = \frac{c_p \mu_t}{\sigma} \tag{5}$$

where c_p, μ_t, and σ are the specific heat capacity, the turbulent viscosity, and the turbulent Prandtl number, respectively. The effective shear-stress tensor is expressed as

$$\left(\tau_{ij}\right)_{eff} = \mu_{eff}\left(\frac{\partial u_i}{\partial x_i} + \frac{\partial u_i}{\partial x_j}\right) - \frac{2}{3}\mu_{eff}\frac{\partial u_k}{\partial x_k}\delta_{ij} \tag{6}$$

where the effective viscosity is

$$\mu_{eff} = \mu + \mu_t \tag{7}$$

The turbulent viscosity is calculated using the standard k-ε model as

$$\mu_t = c_\mu \rho \frac{k^2}{\varepsilon} \tag{8}$$

where k is the turbulent kinetic energy, and ε is the specific dissipation rate. k and ε are

$$\frac{\partial}{\partial t}(\rho k) + \frac{\partial}{\partial x_i}(\rho k u_i) = \frac{\partial}{\partial x_j}\left[\left(\mu + \frac{\mu_t}{\sigma_k}\right)\frac{\partial k}{\partial x_j}\right] + G_k + G_b - \rho\varepsilon + S_k \tag{9}$$

and

$$\frac{\partial}{\partial t}(\rho \varepsilon) + \frac{\partial}{\partial x_i}(\rho \varepsilon u_i) = \frac{\partial}{\partial x_j}\left[\left(\mu + \frac{\mu_t}{\sigma_\varepsilon}\right)\frac{\partial \varepsilon}{\partial x_j}\right] + C_{1\varepsilon}\frac{\varepsilon}{k}(G_k + C_{3\varepsilon}G_b) - C_{2\varepsilon}\frac{\varepsilon^2}{k} + S_\varepsilon \tag{10}$$

where G_k is the turbulent kinetic energy generation associated with mean velocity gradients, while G_b denotes the corresponding generation due to buoyancy. S_k and S_ε are user-defined source terms. The standard model constants c_μ, $C_{1\varepsilon}$, $C_{2\varepsilon}$, σ_k, σ_ε, and σ_T were taken as 0.09, 1.44, 1.92, 1.0, 1.3, and 0.85, respectively [34].

For the PCM region, the phase-change model was formulated assuming a Newtonian and laminar liquid phase. The Boussinesq approximation was applied to account for natural convection. The thermophysical properties of the PCM were considered constant throughout the analysis. Heat transfer and phase-change processes of the PCM were represented using the enthalpy–porosity approach [35]. The effects of thermal expansion and volume changes associated with melting and solidification were neglected, as was the potential formation of voids within the PCM. Furthermore, ideal thermal contact was assumed at the interface between the aluminum receiver walls and the PCM, and the additional thermal contact resistance was neglected. As the PCM melts and its volume decreases slightly, a small air gap forms at the interface between the PCM layer and the insulation layer due to gravity. The resulting thermal contact resistance helps reduce heat losses. Since neglecting this thermal contact resistance results in calculated heat losses that are higher than those that would occur in reality, neglecting this resistance at the initial stage is acceptable.

The governing equations for the PCM region are

$$\frac{\partial(\rho)}{\partial t} + \frac{\partial}{\partial x_i}(\rho u_i) = 0 \tag{11}$$

$$\frac{\partial(\rho u_i)}{\partial t} + \frac{\partial}{\partial x_i}\left(\rho u_i u_j\right) = \mu\frac{\partial u_i}{\partial x_{jj}} - \frac{\partial p}{\partial x_i} + \rho\beta g_i\left(T - T_{ref}\right) + S_i \tag{12}$$

and

$$\frac{\partial(\rho H)}{\partial t} + \frac{\partial}{\partial x_i}[u_i\rho H] = \frac{\partial}{\partial x_j}\left[\gamma\frac{\partial T}{\partial x_j}\right] \tag{13}$$

where H is the total enthalpy of the PCM. The total enthalpy consists of sensible and latent components:

$$H = h + \Delta H \tag{14}$$

The sensible enthalpy is

$$h = h_{ref} + \int_{T_{ref}}^{T} c_p dT \tag{15}$$

The latent enthalpy is defined by

$$\Delta H = \beta L \tag{16}$$

where β is the liquid fraction, and L is the latent heat of the PCM. The liquid fraction is defined according to the PCM temperature as

$$\beta = \begin{cases} \frac{\Delta H}{L} = 0 \;\; if \; T < T_{solid} \\ \frac{\Delta H}{L} = 1 \;\; if \; T > T_{liquid} \\ \frac{\Delta H}{L} = \frac{T - T_{solid}}{T_{liquid} - T_{solid}} \;\; if \; T_{solid} < T < T_{liquid} \end{cases} \tag{17}$$

The liquid fraction, which represents the proportion of the PCM in the liquid state, varies from 0 to 1. A liquid fraction of 0 indicates that the PCM is completely solid, whereas a liquid fraction of 1 indicates that it is completely liquid. Accordingly, complete melting is defined as the state in which the liquid fraction reaches 1, while complete solidification is defined as the state in which the liquid fraction reaches 0.

The momentum source term associated with the mushy region is defined as

$$S_i = C\left(1-\beta^2\right)^2 + \frac{u_i}{\beta^3+\epsilon} \tag{18}$$

C represents the mushy-zone constant, while ϵ denotes a small numerical term introduced to prevent division by zero. In the present study, C was set to 10^5 based on the validation procedure used for the PCM model [36,37].

Finally, heat conduction through the solid receiver layers was modeled using [38]

$$\rho c\frac{\partial T}{\partial t} = \frac{\partial}{\partial x_i}\left(\gamma\frac{\partial}{\partial x_i}\right) \tag{19}$$

Here, ρ is the density, c_p is the specific heat capacity, and γ represents the thermal conductivity of the solid material.

2.4. CFD Modeling

The thermal behavior of the proposed PCM-integrated cavity receiver was investigated using three-dimensional transient CFD simulations in Ansys Fluent v23 R2. The computational domain consisted of the heat transfer fluid (HTF) channel, aluminum receiver wall, PCM layer, and the air/insulation layer. The model accounted for convective heat transfer between the receiver wall and HTF, solar radiation absorption at the receiver inner cavity surfaces, heat conduction through the receiver wall and glass, convective heat transfer in the air within the cavity region situated between the inner cavity walls and glass, convection heat transfer in insulation layer, heat transfer from external receiver surfaces to ambient air, and the transient melting and solidification of the phase-change material. The model also accounted for natural convection in the liquid PCM.

A pressure-based solver was used to perform the CFD simulations. The equations of flow and heat transfer were solved using the coupled solution approach. The energy equation was included in the solution to account for the conjugate heat transfer process between the HTF, receiver walls, PCM, and receiver outer layer. The solidification-melting model in Fluent was applied for solving the PCM layer. The standard k-ε turbulence model was employed to describe the turbulent flow behavior of the HTF. Discrete Ordinates (DO) radiation model was used for the radiative heat transfer within the receiver. All receiver walls were assumed to be opaque. The radiation map shown in Figure 2b was applied to the corresponding cavity inner surfaces to preserve the distribution of the solar heat flux. The non-uniform solar radiation distribution obtained from the optical analysis presented in Section 2.2 was added into the CFD model through a user-defined function (udf). The radiation contribution was included together with convection and conduction in the energy solution of the receiver. For the enclosed insulation (air) layer, the Boussinesq approach was used to account for buoyancy-driven natural convection. Gravity was defined as 9.81 m/s^2 in the -y direction. The external surfaces of the receiver were subjected to convective heat transfer (heat loss) with the ambient air using the surface-specific average heat transfer coefficient obtained from the separate external air simulations.

A closed-loop HTF circulation was adopted in the transient simulations. Water leaving the receiver outlet was recirculated to the inlet, and an approximately 5 °C temperature increase during each circulation cycle was prescribed. Thus, the water entered the receiver initially at 300 K, was heated as it passed through the receiver, and the outlet stream was subsequently returned to the inlet for the next circulation cycle. Accordingly, the required HTF mass flow rate was determined as

$$\dot{m} = \frac{\dot{Q_{abs}}}{c_p\Delta T} \tag{20}$$

Here, $\dot{Q}_{abs}$ denotes the total absorbed solar power, c_p represents the specific heat of water, and ΔT corresponds to the prescribed temperature increase of the HTF per circulation cycle. The resulting water mass flow rate used in CFD simulations was 0.1175 kg/s.

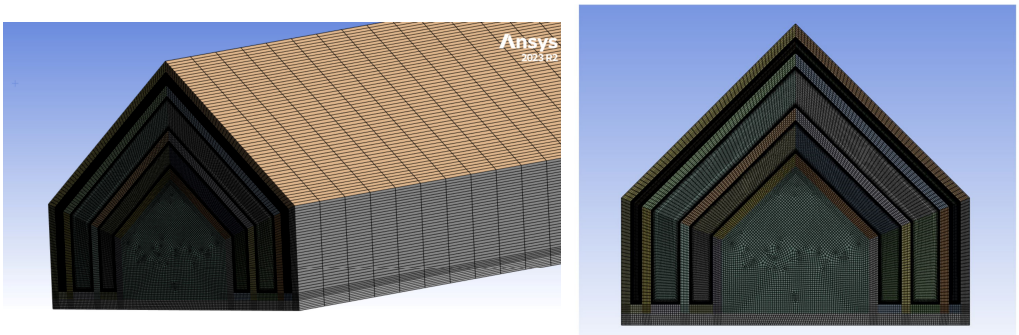
High-density polyethylene (HDPE) was selected as the PCM based on its thermal stability and suitability for medium temperature thermal energy storage applications. The freezing and melting temperatures of HDPE are 120 °C and 130 °C, respectively. Its latent heat is 255,000 J/kg [39,40]. The thermophysical properties assigned to the materials in the numerical model are listed in Table 1. The properties of all materials in Table 1 were assumed to be constant throughout the simulations. The thermophysical properties of PCM and water do not change significantly within the operating temperature range determined in the study. Therefore, temperature-dependent variations in these properties were not considered in the present numerical model.

Table 1. Thermophysical properties of materials.

Material	Density (kg/m^3)	Specific Heat Capacity (J/kg·K)	Thermal Conductivity (W/m·K)	Dynamic Viscosity (Pa·s)
Water	996.54	4183	0.60024	85.338×10^{-5}
HDPE	952	2600	0.48	0.0375
Air	1.225	1006.43	0.0242	1.7894×10^{-5}
Aluminum	2719	871	202.4	-
Glass	2225	835	1.4	-

Initially, the temperature of the system was 300 K. The transient simulations were performed using a 1 s time step. During the charging stage, the non-uniform solar radiation distribution obtained from the optical analysis was applied to the cavity inner surfaces through the udf. After complete melting of the HDPE, the solar heat flux boundary condition was removed to represent the interruption in direct solar irradiation. The cooling and solidification processes were then calculated using the same transient CFD model.

The computational mesh of the final receiver is presented in Figure 3. A mesh independence analysis was performed to determine an appropriate mesh density for transient simulations. The water outlet temperature at the time of complete HDPE melting was used as the comparison criterion. Three mesh densities of approximately 1.8, 2.6, and 3.7 million elements were evaluated. The results obtained from different meshes are presented in Table 2.



(**a**) (**b**)

Figure 3. Computational mesh generated for the PCM-integrated, self-insulated cavity receiver: (**a**) Receiver in perspective view. (**b**) Receiver in front view.

Increasing the mesh refinement from approximately 2.6 to 3.7 million elements changed the HTF temperature by only 0.66 K, corresponding to approximately 0.15%. Therefore, the

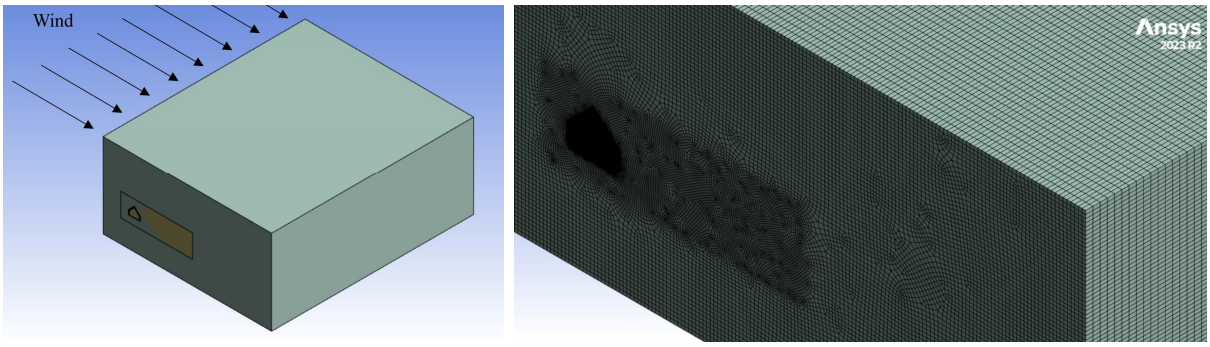
mesh containing 2.6 million elements with a maximum skewness of 0.72 was considered sufficiently mesh-independent and was selected for the transient simulations.

Table 2. Results of the mesh independence analysis.

Mesh Size (Million)	HTF Outlet Temperature (K)
1.8	434.81
2.6	437.52
3.7	438.18

Solving this complex problem, which has a non-uniform radiation map, flow, heat transfer, and melting and solidification, within a single model is highly complicated and computationally expensive. A two-stage CFD solution approach was employed to determine the heat transfer from the receiver external surfaces to the environment and to solve the transient model of the PCM-integrated, self-insulated cavity receiver [41]. In the first stage, the receiver with the external airflow around it was solved at a constant PCM temperature under steady-state conditions to determine the convective heat transfer coefficient for each external cavity surface. In the second stage, the heat transfer coefficients obtained in the first stage were applied as boundary conditions to the external surfaces of the receiver, and a transient CFD solution was performed as planned.

For the external air analysis, a rectangular air domain with a height of 0.8 m, a width of 1.6 m, and a length of 2 m was constructed around the receiver. The three-dimensional external air domain and its mesh structure are shown in Figure 4. The external air mesh contained approximately 3.4 million elements, with a maximum skewness of 0.65.



(**a**) (**b**)

Figure 4. External air domain: (**a**) Three-dimensional external air computational domain surrounding the cavity receiver. (**b**) Computational mesh of the system.

The external airflow was solved as a steady-state forced convection problem under the prescribed conditions. On 18 July 2023 in Etimesgut, Ankara, the ambient temperature was 30.4 °C, with a wind speed of 2.4 m/s. The analysis was performed for four representative PCM temperatures of 50, 80, 100, and 130 °C, which was PCM melting temperature. Four different temperatures were selected to represent the process of PCM melting. Each external surface had different heat transfer coefficients. The locations and numbering of the external receiver plates are presented in Figure 5.

Analyses were performed for each temperature, and four different heat transfer coefficients were obtained for each surface. The average of the four values obtained for each plate was calculated (Table 3) and used as a boundary condition for the transient CFD analysis.

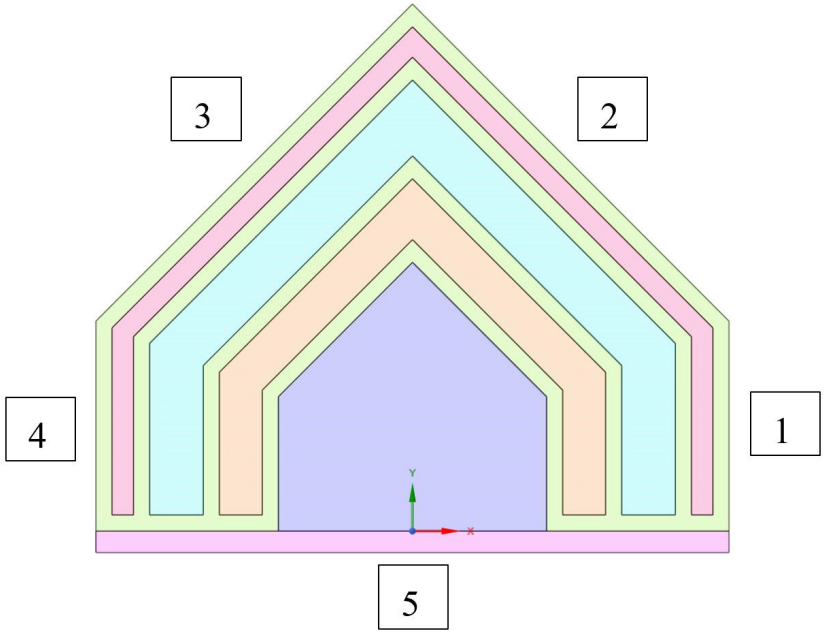


Figure 5. Numbering of the external receiver surfaces considered in the convective heat transfer analysis.

Table 3. Average heat transfer coefficients for the external surfaces.

Surface	Average Heat Transfer Coefficient (W/m^2K)
1	10.59
2	16.22
3	14.83
4	22.74
5	10.33

2.5. Model Validation

The proposed receiver is difficult to directly validate against a single experimental system in the literature because of its novel geometry and the simultaneous consideration of multiple physical processes. Therefore, two complementary validation models representing the fundamental physical components of the developed numerical model were employed. The first validation was performed using an LS-2 parabolic trough collector–receiver model representing HTF flow and conjugate heat transfer under non-uniform solar irradiation. The second validation was conducted using an experimentally investigated PCM system representing the transient thermal and phase-change behavior of the PCM.

For the first validation, the LS-2 collector experimentally investigated by Dudley et al. [42] was considered. The HTF region, absorber tube, and glass envelope were modeled. Heat conduction within the solid regions was taken into account. The experimental results were shown in Table 4.

Table 4. Experimental operating conditions for LS-2.

Parameter	Value
Wind speed (m/s)	3.6
HTF inlet temperature (K)	374.35
HTF outlet temperature (K)	392.15
Direct solar irradiation (W/m^2)	813.1
HTF mass flow rate (kg/s)	0.7254
Ambient air temperature (K)	298.95

The non-uniform solar radiation distribution obtained from SolTrace over the absorber surface was transferred to Ansys Fluent through a udf. The Discrete Ordinates (DO) radiation model was applied to solve radiative heat transfer. All solar receiver surfaces were assumed to be opaque, and an emissivity of 0.14 was assigned to the absorber surface. The external convection heat transfer coefficient was calculated as [34]

$$h = 4V^{0.58}D^{-0.42} \quad (21)$$

where V is the wind speed, and D is the outer diameter of the glass envelope. The calculated heat transfer coefficient was 20.8556 W/m^{2}K.

The thermophysical properties of Syltherm 800 and steel as receiver material were shown in Table 5 [34]. The properties of air and glass, which were also used in the model, were given in Table 1. The density of the Syltherm 800 was introduced into the solver as a temperature-dependent piecewise polynomial, whereas the remaining properties were evaluated as constant [34]. Natural convection in the enclosed air region was modeled using the Boussinesq approximation, with buoyancy effects taken into account.

Table 5. Thermophysical properties used in the LS-2 validation model.

Material	Density (kg/m^3)	Specific Heat Capacity (J/kg·K)	Thermal Conductivity (W/m·K)	Dynamic Viscosity (Pa·s)
Syltherm 800	polynomial	1762	0.1181	0.0027
Steel	8030	502	16.27	-

Using a mesh consisting of approximately 2.7 million elements, the calculated HTF outlet temperature was 394.38 K. The experimental outlet temperature reported by Dudley et al. [42] was 392.15 K, corresponding to a relative difference of 0.57% between the experimental and numerical results.

The second validation was performed using a PCM melting system experimentally investigated by Al-Abidi et al. [43]. In the system, the region between concentric copper tubes was filled with RT82 as PCM. Water was circulated through the tubes to initiate PCM melting. The inner tube heating configuration was selected for the present validation. An initial RT82 temperature of 300 K, HTF inlet temperature of 363 K, and a water mass flow rate of 2.4 kg/min were specified. The thermophysical properties of the materials were presented in Table 6 [33]. The thermophysical properties of water, which was also used in the analysis, were given in Table 1. The freezing and melting temperatures of RT82 are 343.27 K and 355.32 K, respectively. Its latent heat is 210,643 J/kg [43].

Table 6. Thermophysical properties used in the PCM validation model.

Material	Density (kg/m^3)	Specific Heat Capacity (J/kg·K)	Thermal Conductivity (W/m·K)	Dynamic Viscosity (Pa·s)
RT82	950	2000	0.2	0.03499
Copper	8978	381	387.6	-

The transient melting behavior of the RT82 was modeled using the finite volume method. A 1 s time step was used, with 20 iterations performed at each step. The numerically obtained PCM temperature was compared with the experimental data. At approximately 171 min, the experimental PCM temperature was 354.66 K, whereas the numerical value was

343.45 K. The maximum temperature difference was 11.21 K, and the maximum relative error was 3.16%. The comparison of the experimental and numerical temperature is presented in Figure 6.

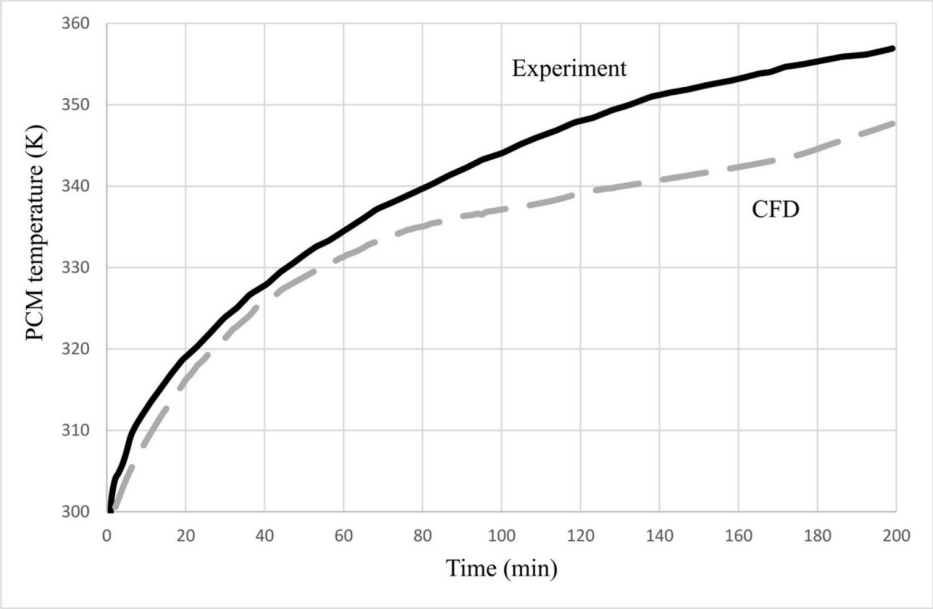


Figure 6. Comparison of experimental and CFD results for PCM temperature.

Through these two complementary validation studies, the novel solar receiver model was validated with respect to all the physical processes incorporated into the model.

3. Results

3.1. PCM Melting and Solidification

The transient thermal behavior of the PCM-integrated cavity receiver was first evaluated under solar irradiation. The simulation was initiated at 300 K. The water temperature, HDPE temperature, and liquid fraction were monitored throughout the charging process.

HDPE started melting after approximately 13 min and melted completely at 1876 s, corresponding to approximately 31 min. At complete melting, the water outlet temperature reached 437.54 K. In Figure 7, the receiver's temperature distribution during the melting process is presented. The results showed that both the HTF and HDPE temperatures increased progressively as the absorbed solar energy was transferred through the receiver. The water outlet temperatures at 5, 10, 15, 20, 25, and 30 min were 347, 382, 407, 416, 423, and 433 K, respectively. The HDPE temperatures were 338, 373, 394, 398, 404, and 418 K. At complete melting, the average HDPE temperature reached 423.76 K. When solar radiation was absorbed by the wall of the cavity inner surfaces, it was an expected result that the HDPE temperature was lower than that of the water, given that the water forms the first layer of the receiver.

Time-dependent liquid fraction distribution for HDPE melting is shown in Figure 8. The melting process was non-uniform throughout the HDPE layer because of the non-uniform heat flux distribution. The liquid region increasingly expanded as the charging process continued, while the remaining solid HDPE was concentrated in regions exposed to relatively lower thermal input. The uppermost region of the cavity was seen as the last region to melt. This non-uniform melting behavior was a direct consequence of the heterogeneous thermal loading of the cavity, and it demonstrated that the local radiation distribution plays an important role in the PCM charging process.

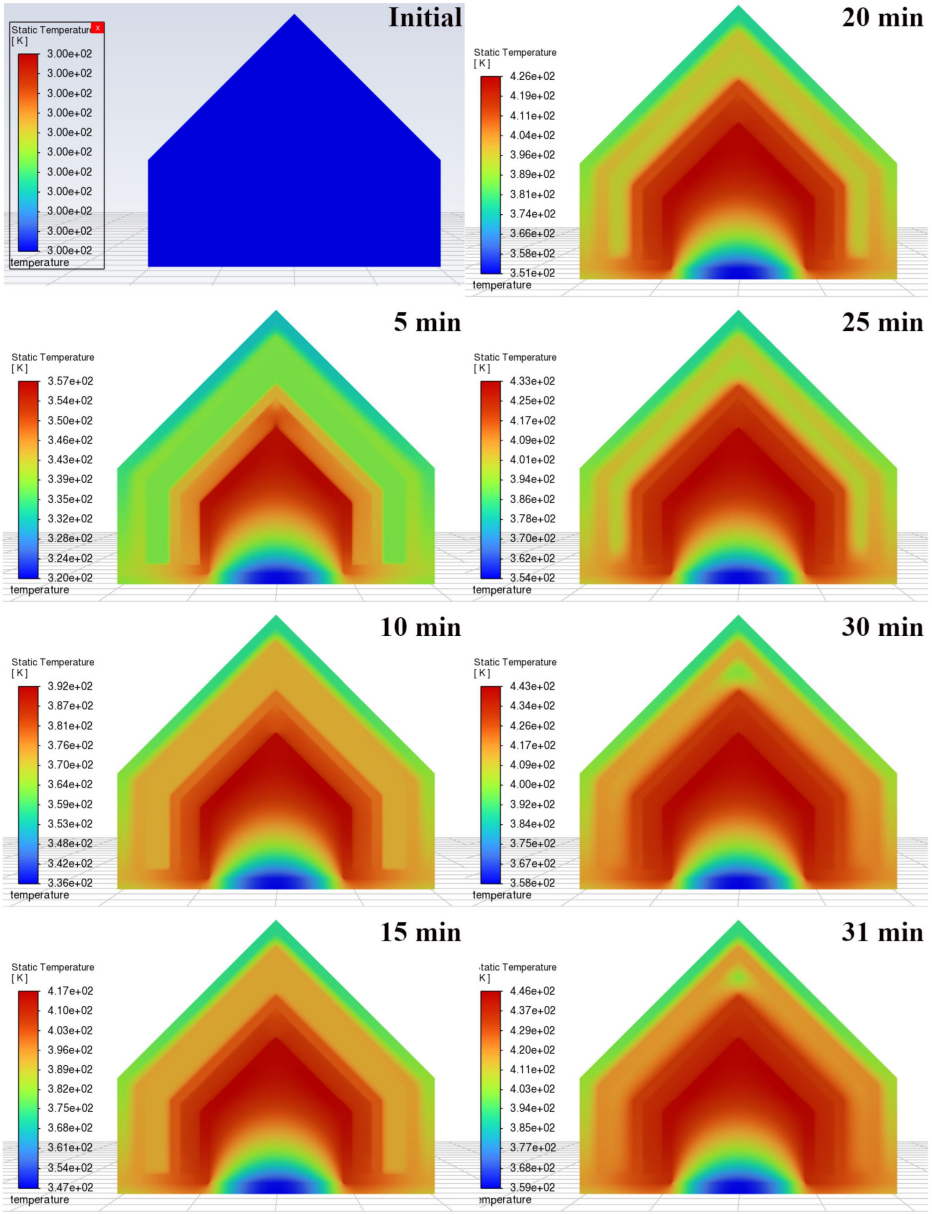


Figure 7. Transient temperature distribution of the receiver during PCM melting.

Figures 9 and 10 present the liquid fraction and water outlet temperature, respectively. Liquid fraction values vary between 0 and 1, where a value of 0 represents the state in which the entire volume is solid, and a value of 1 represents the state in which it is entirely liquid. The liquid fraction remained close to zero during the initial heating period and began to increase significantly after approximately 13 min. It subsequently increased continuously until reaching 1 at 1876 s. Accordingly, the water outlet temperature increased progressively.

After complete HDPE melting, the solar radiation boundary condition was removed to represent a temporary interruption in direct solar irradiation. The state at the end of the charging period was taken as the initial condition for the subsequent solidification analysis.

The transient liquid fraction distribution in the receiver during solidification is presented in Figure 11. Solidification initially occurred near the lower cavity walls, where heat losses to the surroundings were comparatively higher. As cooling progressed, solidification developed from both the upper and lower boundaries because heat was transferred simultaneously toward the outer layer and the water. The liquid region progressively decreased until the HDPE became completely solid.

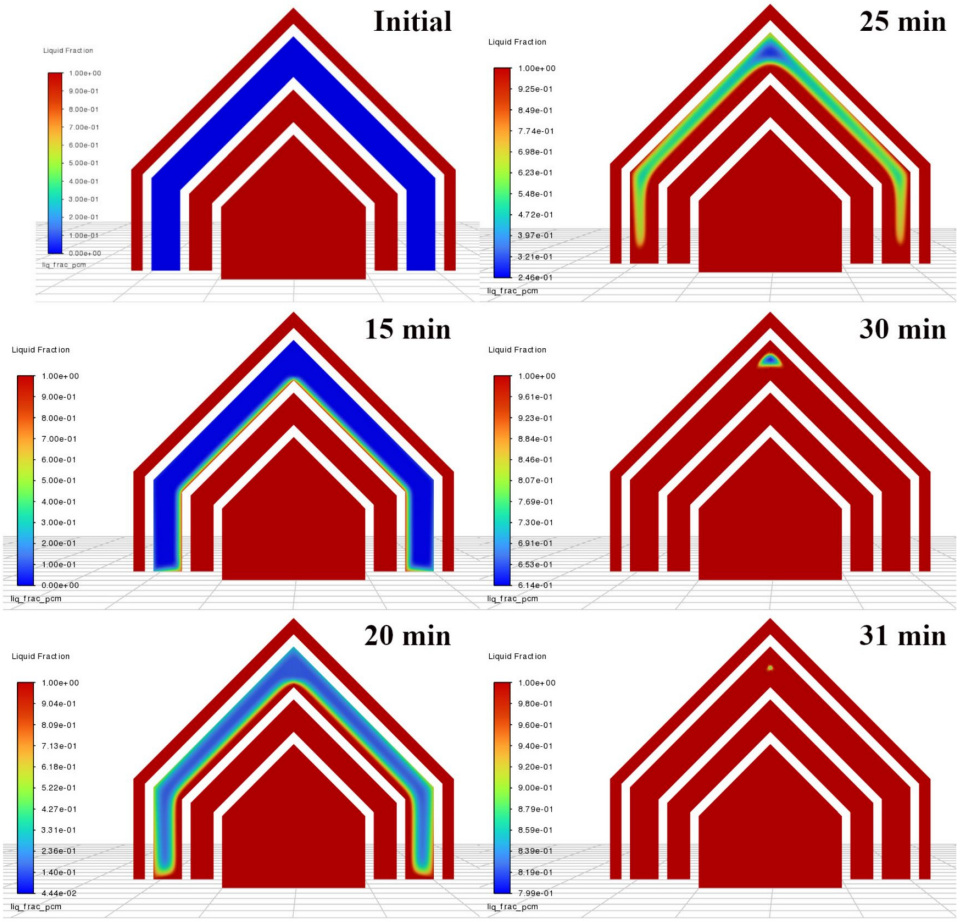


Figure 8. Transient liquid fraction distribution during HDPE melting.

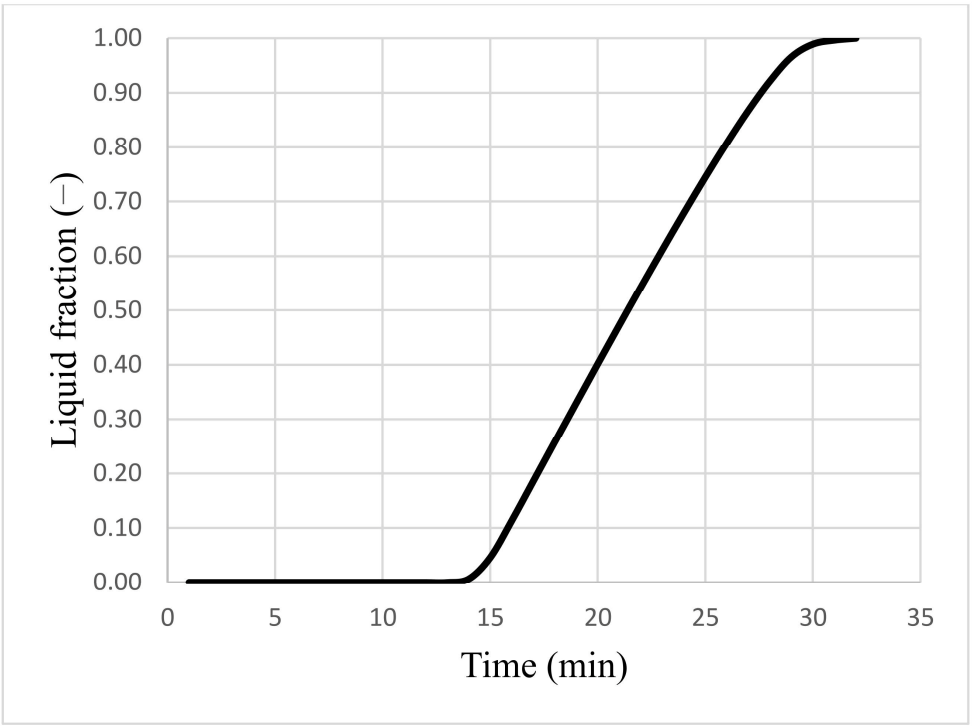


Figure 9. Liquid fraction during HDPE melting.

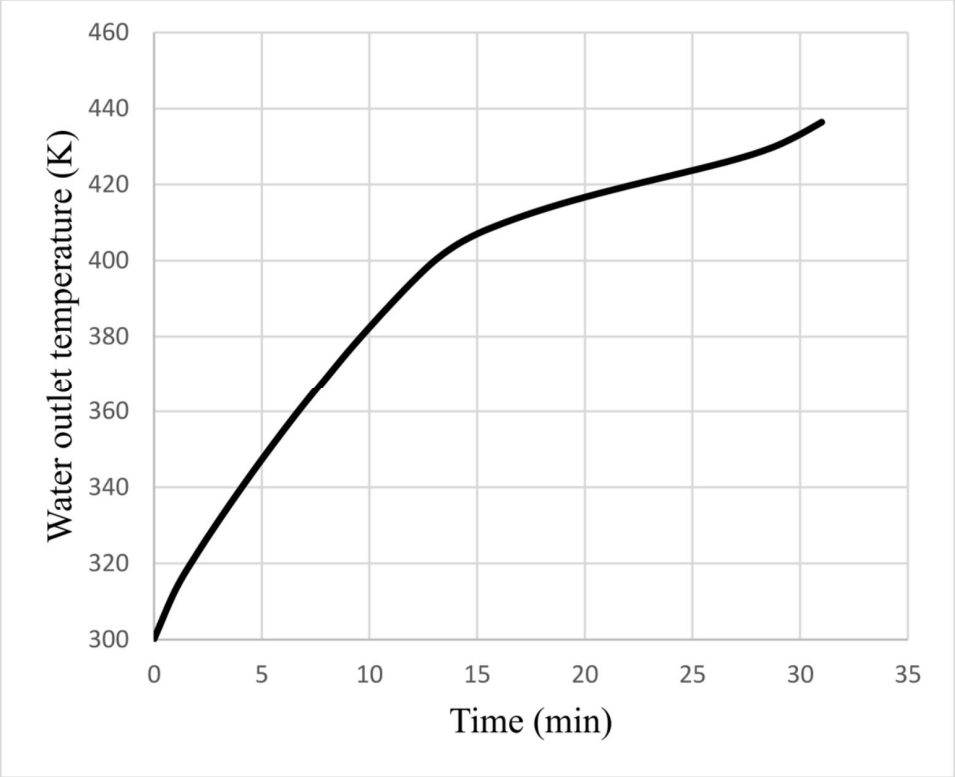


Figure 10. Water outlet temperature during HDPE melting.

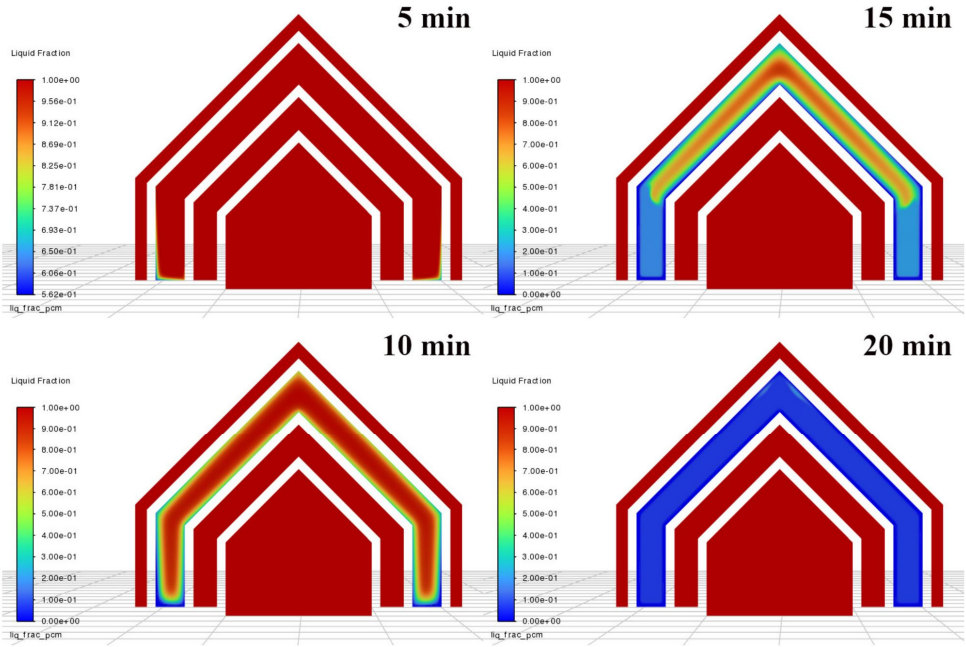


Figure 11. Transient liquid fraction distribution during HDPE solidification.

The transient distribution of the outlet temperature of water and liquid fraction is presented in Figures 12 and 13. The HDPE started to solidify approximately 5 min after the interruption and reached complete solidification at 21 min, resulting in a solidification period of about 16 min. During this phase-change period, the water temperature remained relatively stable, which is characteristic of the latent heat release associated with solidification.

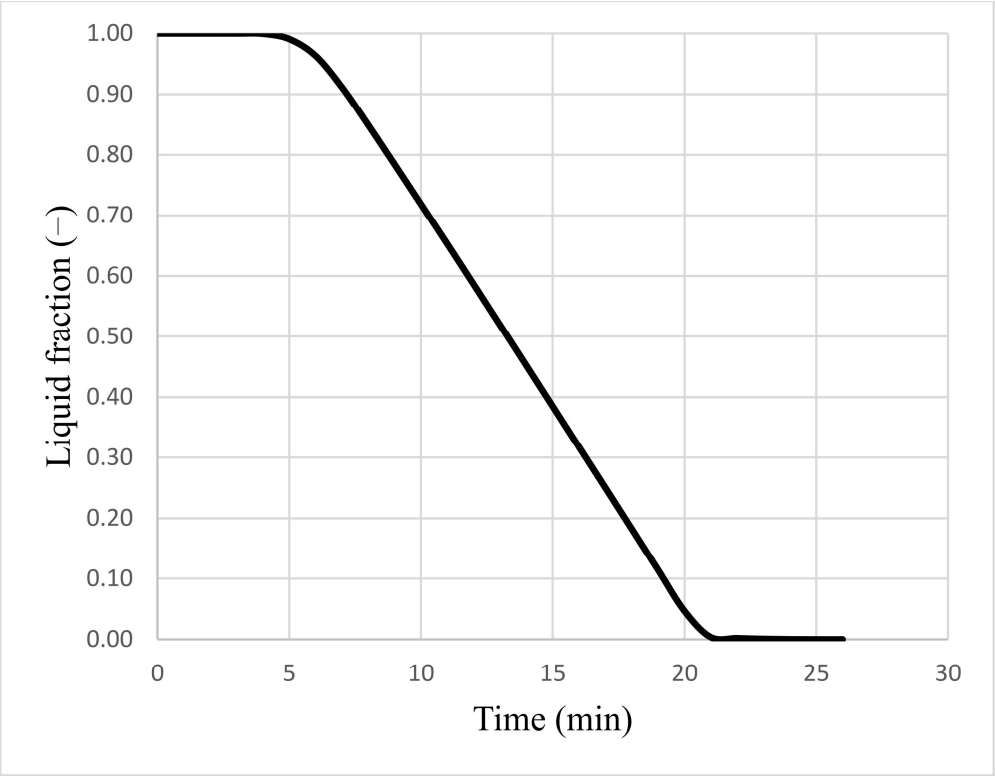


Figure 12. Liquid fraction during HDPE solidification.

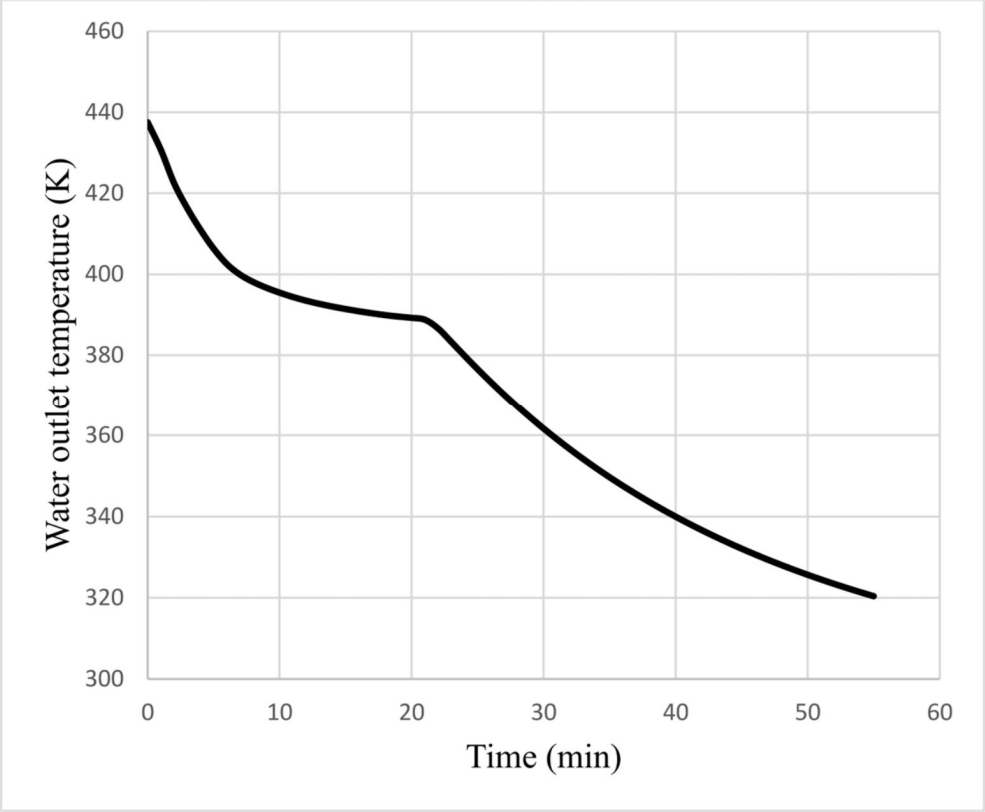


Figure 13. Water outlet temperature during HDPE solidification.

3.2. Comparison with the Receiver Without PCM

To discuss the contribution of PCM integration, the proposed novel receiver was compared with an otherwise comparable simple cavity receiver. This simple receiver only had an 8 mm thick HTF layer. It had no PCM or insulation layer.

The cross-sectional geometry and dimensions of the non-PCM receiver and its mesh refinement are presented in Figure 14. The non-PCM and PCM-integrated receivers have the same cavity dimensions (50 mm × 50 mm), HTF channel thickness (8 mm), aluminum wall thickness (3 mm), and low-iron glass thickness (4 mm). However, the non-PCM receiver does not contain the HDPE and the insulation layer. Consequently, its outer width and height are 78 mm and 69.8 mm, respectively. The meteorological conditions, operating conditions, and HTF (water) conditions and properties were kept identical for both receivers. The distribution of the concentrated solar radiation obtained from SolTrace for non the non-PCM receiver was the same as that shown for the PCM-integrated receiver in Figure 2b. However, because the non-PCM receiver has a narrower cross-section (78 mm), it causes less optical shading of the collector, resulting in a slightly higher absorbed solar power of 2521 W, compared with 2458 W for the PCM-integrated receiver. The analyses were conducted under the same operating conditions for both solar irradiation and solar interruption conditions and the same boundary conditions. The initial system temperature and the water inlet temperature are taken as 300 K.

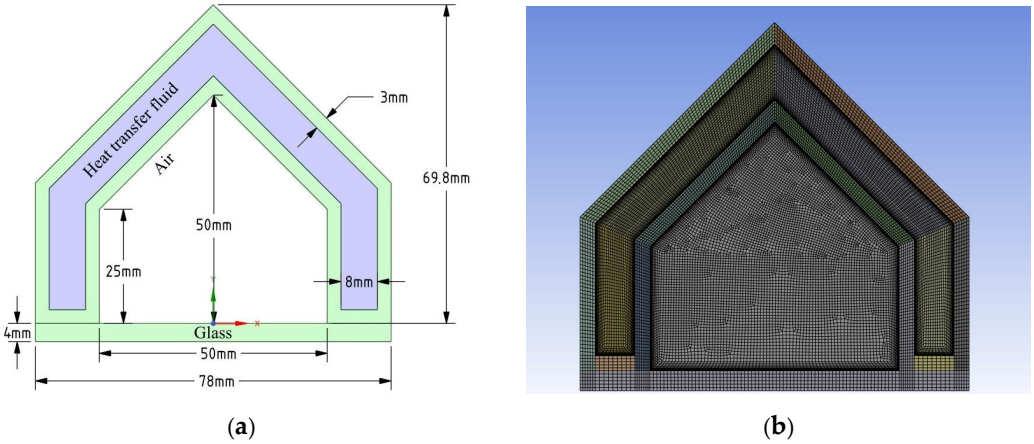


Figure 14. Physical configuration of the non-PCM: (**a**) front view with principal dimensions and layers; (**b**) computational mesh generated for the non-PCM receiver.

Under solar irradiation, the outlet temperature of the water was 437.52 K for the PCM-integrated receiver at the end of the investigated charging period, whereas the simple non-PCM receiver reached 476.38 K for the same period. The corresponding transient water temperature profiles are presented in Figure 15. The PCM-integrated receiver showed a slower temperature rise because part of the absorbed energy was diverted into latent heat storage. From an operational perspective, this behavior should not be evaluated solely as a disadvantage of the PCM configuration. The objective of the PCM layer is to redistribute the absorbed energy over time rather than to maximize the HTF temperature rapidly during solar irradiation.

The comparison under solar interruption conditions is presented in Figure 16. At the beginning of the phase-change period, approximately 5 min after the interruption, the water outlet temperatures of the PCM-integrated and non-PCM receivers were 406.3 and 410.2 K, respectively. By the end of the 16 min solidification period, the corresponding temperatures were 388.8 and 352.2 K, respectively. Therefore, the water outlet temperature

decrease was only 17.5 K for the PCM-integrated receiver, compared with 58 K for the receiver without PCM.

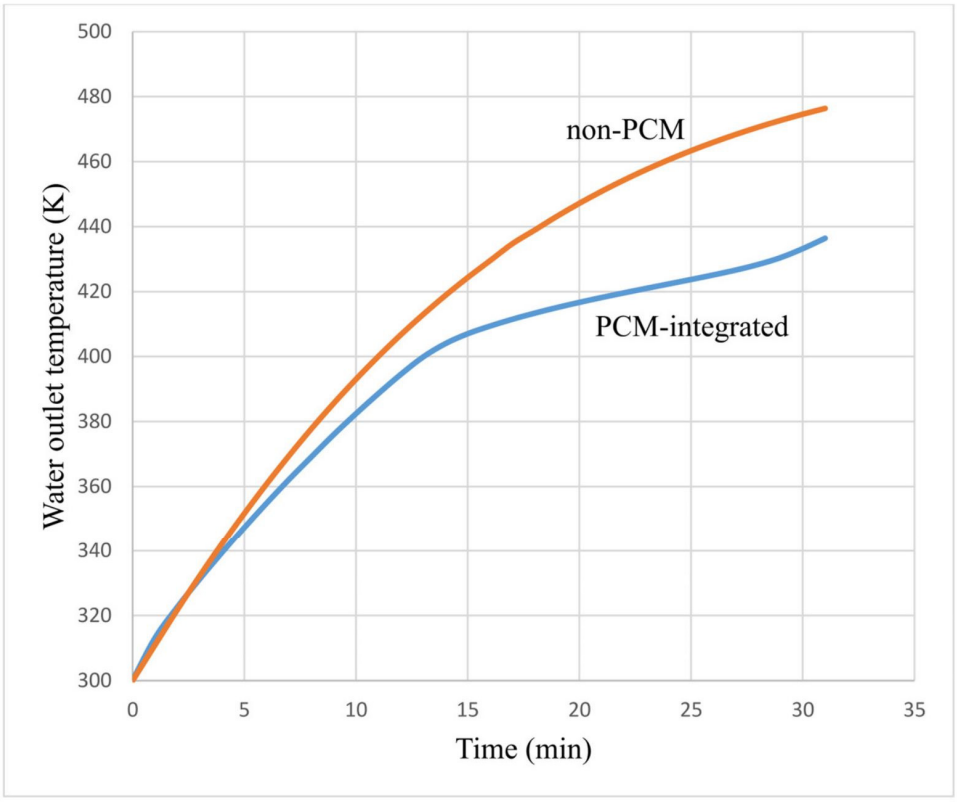


Figure 15. Water outlet temperature of the PCM-integrated and non-PCM cavity receivers under solar irradiation.

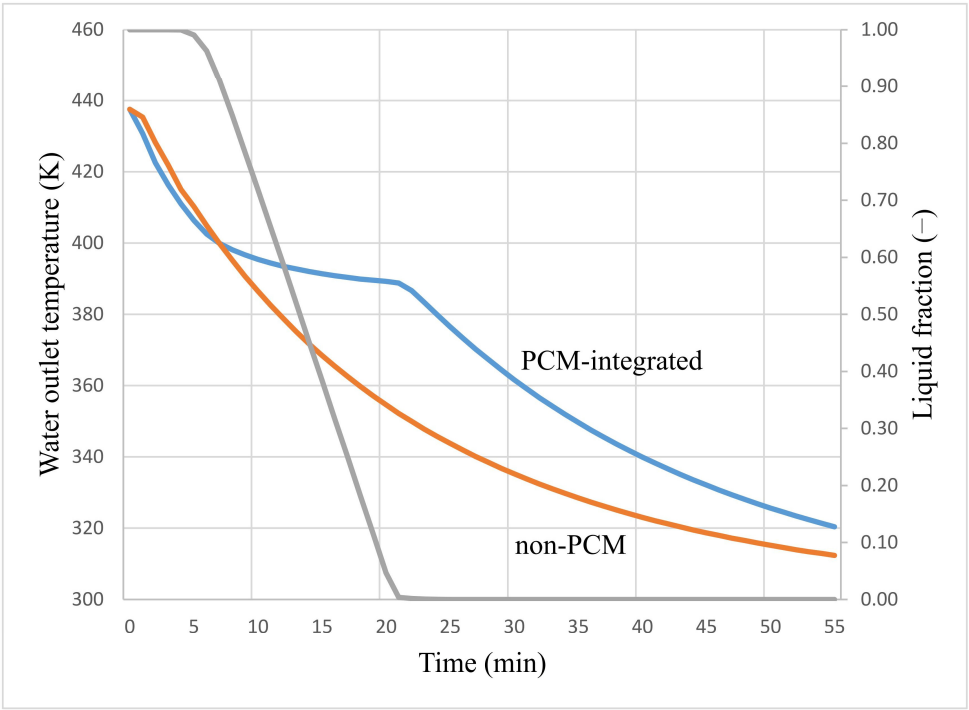


Figure 16. Water outlet temperature of the PCM-integrated and non-PCM cavity receivers during solar irradiation interruption, together with PCM liquid fraction profile.

Thus, the outlet temperature drop was limited to 17.5 K in the PCM-integrated receiver, compared with 58 K in the non-PCM receiver, representing a 69.8% reduction in the temperature decrease. Relative to the water outlet temperature at the onset of solidification, the temperature decrease in the PCM-integrated receiver was approximately 4.3%. The main objective of this study is to ensure that the decrease in HTF outlet temperature remains below 5% during direct irradiance interruptions caused by transient cloud passages. The analyses achieved this target, with a temperature decrease of 4.3%. These results also demonstrate the thermal-buffering effect of PCM integration under transient solar irradiation conditions. The 69.8% reduction in the outlet temperature drop indicates that the HDPE mitigates the decline in water outlet temperature by releasing stored thermal energy during solidification. This behavior limits temperature fluctuations when direct solar irradiation is interrupted, such as during the passage of clouds, and helps maintain greater thermal stability in concentrating solar collector systems.

The reasonably smaller temperature decrease of the PCM-integrated receiver resulted from the release of latent heat during PCM solidification. In contrast, the non-PCM simple receiver responds directly to the removal of the solar heat input, and its water outlet temperature decreases much more rapidly as heat losses to the surroundings continue. The liquid fraction profile shown together with the temperature curves further confirms that the period of reduced temperature decline coincides with the PCM phase-change process.

As a result, the comparison demonstrates that the principal function of the PCM layer is thermal buffering. The stored latent heat moderates the HTF temperature decrease following solar interruption and maintains a higher outlet temperature than the non-PCM configuration over the investigated 16 min period.

The energy balance of the PCM-integrated cavity receiver was evaluated over the charging period required for the HDPE to melt completely. The overall energy balance was expressed as

$$Q_{solar} = Q_{HTF} + Q_{PCM} + Q_{res} \tag{22}$$

where Q_{solar} is the total solar energy absorbed by the cavity, Q_{HTF} is the increase in the thermal energy of the water, Q_{PCM} is the total energy stored in the HDPE as sensible and latent heat, and Q_{res} is the residual energy term. The residual energy term accounts for the thermal losses to the surroundings and any energy stored in the solid receiver components, insulation, and air within the cavity area that is not included in the other energy terms.

The solar power absorbed by the cavity surfaces was 2458 W. Over the 1876 s charging period required for the HDPE to melt completely, the total absorbed solar energy was 4610 kJ.

The thermal energy absorbed by the water was calculated using the following equation.

$$Q_{HTF} = m_{HTF} c_{p,HTF} \left(T_f - T_i\right)_{HTF} \tag{23}$$

where m_{HTF} is the mass of water in the modeled flow domain. $c_{p,HTF}$ is the specific heat capacity of the water, and T_f and T_i are the final and initial temperatures of water, respectively. The water mass was determined from the volume of the water-flow domain and the density of water. The resulting water mass in the flow domain was 2.237 kg. Since the water circulates in a closed-loop system, this value represents the mass of water contained in the modeled flow domain. The water temperature increased from 300 K to 437.54 K during the charging period. The corresponding increase in the water's thermal energy was calculated as 1287 kJ.

The total energy stored in the PCM comprises sensible and latent heat contributions. The sensible heat storage was calculated as [4]

$$Q_{sensible} = m_{PCM} c_{p,PCM} \left(T_f - T_i\right)_{PCM} \tag{24}$$

Here, m_{PCM} is the mass of HDPE (3.507 kg), $c_{p,PCM}$ is its specific heat capacity, and T_f and T_i are the final and initial PCM temperatures, respectively. Sensible heat storage continues during the melting process because the temperature of the PCM does not remain constant throughout the phase transition. As the liquid fraction increases, the melted portion of the PCM continues to absorb sensible heat as its temperature rises, while latent heat is simultaneously stored through the solid-to-liquid phase transition. At the end of the charging period, the average HDPE temperature was 423.76 K. The calculated sensible heat storage was 1127.2 kJ. The latent heat stored during the phase change was determined as [4]

$$Q_{latent} = m_{PCM}L \tag{25}$$

The resulting latent heat storage was 894.43 kJ. Accordingly, the total energy stored in the PCM was calculated as 2021.4 kJ.

The thermal efficiency during charging is defined as the ratio of the thermal energy gained by the water to the total absorbed solar energy by the receiver. Of the total absorbed solar energy, 27.9% corresponded to the increase in water thermal energy, while 43.9% was stored in the HDPE. Accordingly, the charging thermal efficiency was 27.9%. Sensible heat storage accounted for 24.5% of the absorbed solar energy, whereas latent heat storage accounted for 19.4%. These results indicate that both the temperature increase of the HDPE and its phase transition contributed substantially to energy storage during charging. The remaining 28.2% was attributed to the residual energy term.

Of the total energy stored in the HDPE, 44.2% was in the form of latent heat and 55.8% was in the form of sensible heat. This indicates that both phase-change energy storage and sensible heat storage contributed substantially to total thermal energy stored during charging.

During the 16 min solidification period following the interruption of solar irradiation, the water outlet temperature decrease was 17.5 in the PCM-integrated receiver, compared with 58 K in the non-PCM receiver. This corresponds to a 40.5 K reduction in the temperature decrease, or a 69.8% improvement in outlet temperature drop. This improvement is attributed primarily to the thermal buffering effect of the PCM, including the release of latent heat during solidification. To quantify the energy-equivalent thermal buffering effect relative to the latent heat stored during charging, the latent-heat-related thermal-buffering ratio was defined as follows:

$$R_{latent} = \frac{m_{HTF}c_{p,HTF}(T_{d1} - T_{d2})}{Q_{latent}} \times 100 \tag{26}$$

where T_{d1} and T_{d2} are the outlet temperature drops in the non-PCM (58 K) and PCM-integrated (17.5 K) receivers, respectively. The latent-heat-related thermal-buffering ratio was calculated as 42.4%, representing the energy equivalent associated with the reduction in the water outlet temperature decrease relative to the latent heat stored in the HDPE during charging. This ratio provides a comparative measure of the thermal buffering effect associated with PCM integration.

4. Discussion

A novel cavity receiver with PCM integration and insulation for a PTC was numerically investigated to characterize its transient thermal energy storage behavior and response to solar irradiation interruption. The findings obtained from the study are summarized below:

- The HDPE began melting after approximately 13 min under the investigated solar irradiation conditions and reached complete melting at 1876 s, approximately 31 min.

- The water outlet temperature reached 437.52 K when the HDPE was completely melted, demonstrating the simultaneous heating of the HTF and charging of the latent heat storage layer.
- The HDPE melting process was non-uniform because of the non-uniform concentrated solar radiation distribution over the cavity inner surfaces. The uppermost region of the cavity was the last region to melt.
- During the charging period, the HDPE stored a total of 2021.4 kJ of thermal energy, comprising 1127.2 kJ of sensible heat and 894.43 kJ of latent heat. Sensible heat accounted for 55.8% of the total energy stored in the HDPE, while latent heat accounted for 44.2%.
- Following solar irradiation interruption, HDPE solidification began after approximately 5 min and was completed at approximately 21 min, corresponding to a solidification period of about 16 min.
- During the solidification period, the water outlet temperature decreased by only 17.5 K. This limited temperature decrease demonstrated the thermal buffering effect of the latent heat released by the HDPE during solidification.
- In the corresponding non-PCM simple cavity receiver, the water outlet temperature decreased by 58 K. Thus, the PCM-integrated receiver maintained a higher outlet temperature following solar irradiation interruption.
- The water outlet temperature decrease was reduced by 69.8% in the PCM-integrated receiver compared with the non-PCM receiver. Relative to the water outlet temperature at the onset of solidification, the 17.5 K decrease in the PCM-integrated receiver corresponded to only 4.3%.
- The latent-heat-related thermal-buffering ratio was estimated at 42.4%, indicating the energy-equivalent contribution associated with the reduction in the water outlet temperature decrease relative to the latent heat stored in the HDPE.
- The comparison indicated that the primary contribution of PCM integration was thermal buffering rather than an increase in instantaneous outlet temperature during the charging process. The stored latent heat was released during solidification and reduced HTF temperature fluctuations following temporary solar interruptions.

The numerical results showed that the proposed PCM-integrated cavity receiver can provide short-term latent thermal energy storage and can moderate HTF outlet temperature reductions following temporary interruptions in direct solar irradiation. The configuration therefore provides a potential approach for improving the transient thermal stability of parabolic trough solar thermal systems exposed to short-duration solar interruptions.

Although the present study demonstrates the thermal-buffering capability of the proposed patented cavity receiver under the investigated operating conditions, further investigations under a comprehensive range of practical operating scenarios would be valuable. In particular, the effects of partial PCM melting, repeated cloud passages, variable solar irradiance, different HTFs and flow rates, and consecutive daily operating cycles could be examined in future studies. Such investigations could provide further insight into the receiver's dynamic response under intermittent solar irradiation, the repeatability of its thermal buffering performance, and the influence of operating conditions on PCM charging and discharging behavior.

Beyond its thermal energy storage capability, the proposed PCM-integrated receiver offers potential system-level benefits by moderating temperature fluctuations during interruptions in solar irradiation. The incorporation of the PCM layer and its containment increase the receiver's overall mass and volume compared with the receiver without PCM. These additional material requirements should be considered when evaluating the design practical implementation. During the investigated 16 min solidification period, the outlet

temperature decrease was 17.5 K for the PCM-integrated receiver, compared with 58 K for the non-PCM receiver. This reduced temperature variation may help mitigate repeated thermal loading of receiver components and could contribute to more stable thermal operation under intermittent solar input. Furthermore, by storing thermal energy during solar irradiation and releasing it during interruptions, the PCM-integrated receiver supports a more temporally balanced utilization of the absorbed solar energy and helps maintain thermal output when direct solar irradiance input is unavailable. Future investigations could examine these aspects, including the relationship between reduced temperature fluctuations and thermal stress development, its performance under different irradiance and conditions, the hydraulic and geometric implications of the additional PCM layer and containment, the economic implications of the added materials and manufacturing requirements, and the stability of HDPE properties under repeated melting and solidification cycles.

5. Patents

The receiver concept investigated in this study is protected by Turkish Patent No. 2021/013862, entitled "Cavity Solar Receiver Containing Phase Change Material".

Author Contributions: Conceptualization, G.A. and L.Ç.; methodology, G.A. and L.Ç.; validation, G.A. and L.Ç.; formal analysis, G.A. and L.Ç.; investigation, G.A. and L.Ç.; writing—original draft preparation, G.A. and L.Ç.; writing—review and editing, G.A. and L.Ç.; visualization, G.A. and L.Ç.; supervision, G.A. and L.Ç.; project administration, G.A. and L.Ç. All authors have read and agreed to the published version of the manuscript.

Funding: This research was funded by the Scientific and Technological Research Council of Türkiye (TÜBİTAK), grant number 122M039.

Data Availability Statement: The data generated and/or analyzed during the present study can be obtained from the corresponding author upon reasonable request.

Conflicts of Interest: The authors declare no conflicts of interest.

References

1. Sharma, A.; Tyagi, V.V.; Chen, C.R.; Buddhi, D. Review on thermal energy storage with phase change materials and applications. *Renew. Sustain. Energy Rev.* **2009**, *13*, 318–345. [CrossRef]
2. Xu, B.; Li, P.; Chan, C. Application of phase change materials for thermal energy storage in concentrated solar thermal power plants: A review to recent developments. *Appl. Energy* **2015**, *160*, 286–307. [CrossRef]
3. Nagar, S.; Sreenivasa, S. Thermal performance investigations by the use of nanofluids and phase change materials (PCM) in parabolic trough collectors (PTC) along with exergetic, economic, and application-based analyses. *Proc. Inst. Mech. Eng. Part A J. Power Energy* **2025**, *239*, 1119–1142. [CrossRef]
4. Guerraiche, D.; Bougriou, C.; Guerraiche, K.; Valenzuela, L.; Driss, Z. Experimental and numerical study of a solar collector using phase change material as heat storage. *J. Energy Storage* **2020**, *27*, 101133. [CrossRef]
5. Senthil, R.; Cheralathan, M. Enhancement of the thermal energy storage capacity of a parabolic dish concentrated solar receiver using phase change materials. *J. Energy Storage* **2019**, *25*, 100841. [CrossRef]
6. Togun, H.; Basem, A.; Mohammed, H.I.; Biswas, N.; Abed, A.M.; Rashid, F.L.; Maarof, H.A.; Hamdi, J.D.; Hussein, A.K.; Paul, D. Harnessing solar energy with phase change materials: A review of melting point impacts. *Int. Commun. Heat Mass Transf.* **2025**, *165*, 109094. [CrossRef]
7. Bashir, M.A.; Giovannelli, A. Design optimization of the phase change material integrated solar receiver: A numerical parametric study. *Appl. Therm. Eng.* **2019**, *160*, 114008. [CrossRef]
8. Senthil, R. Effect of charging of phase change material in vertical and horizontal rectangular enclosures in a concentrated solar receiver. *Case Stud. Therm. Eng.* **2020**, *21*, 100653. [CrossRef]
9. Mohammad, S.I.; Vasudevan, A.; Alkhuzai, K.A.; Abu Zneid, B.; Reddy, M.S.; Thakur, V.; Kumar, R.; Singh, A.; Roshn, I. Transient thermo-optical and phase-change modeling of a parabolic trough solar collector integrated with Al_2O_3 nano-enhanced PCM. *Energy Explor. Exploit.* **2026**, *44*, 2675–2715. [CrossRef]

10. Ebadi, H.; Alarcón-Padilla, D.-C.; Guedez, R.; Mahmoudi, H.; Trevisan, S.; Valenzuela, L.; Savoldi, L. Thermal design optimization of a parabolic trough collector receiver with a tube-bundle cavity. *Sol. Energy* **2026**, *309*, 114439. [CrossRef]
11. Chopra, K.; Tyagi, V.V.; Pathak, A.K.; Pandey, A.K.; Sari, A. Experimental performance evaluation of a novel designed phase change material integrated manifold heat pipe evacuated tube solar collector system. *Energy Convers. Manag.* **2019**, *198*, 111896. [CrossRef]
12. Chopra, K.; Pathak, A.K.; Tyagi, V.V.; Pandey, A.K.; Anand, S.; Sari, A. Thermal performance of phase change material integrated heat pipe evacuated tube solar collector system: An experimental assessment. *Energy Convers. Manag.* **2020**, *203*, 112205. [CrossRef]
13. Chakraborty, O. Numerical analysis of fins and nano-enhanced PCM for heat transfer improvement in parabolic trough collectors. *Sol. Energy* **2026**, *303*, 114158. [CrossRef]
14. Anand, S.; Kumar, S. Thermal performance analysis of parabolic trough collectors with gaseous heat transfer fluid and thermal energy storage system. *Appl. Therm. Eng.* **2025**, *279*, 127858. [CrossRef]
15. Mathan, P.; Ponraj, V.; Selvakumar, P.; Armstrong, M. Hybrid sand-PCM thermal energy storage driven with a solar parabolic trough concentrator for enhanced charging–discharging performance. *Energy* **2026**, *344*, 139989. [CrossRef]
16. Hanchi, N.; Elbahjaoui, R.; Faraji, H. Assessment of performance for a finned triplex-tube thermal energy storage system utilizing cascaded latent heat storage materials. *J. Energy Storage* **2026**, *144*, 119715. [CrossRef]
17. Bashir, M.A.; Ali, H.M. Design and analysis of PCM integrated solar receiver with double-helical tube structure. *J. Energy Storage* **2024**, *84*, 110872. [CrossRef]
18. Bagherzadeh, K.; Piroozmand, V.; Ahmadi, R. Cascading latent heat thermal energy storage in parabolic trough solar collector as a promising solution: An experimental investigation. *Energy Convers. Manag.* **2024**, *300*, 117942. [CrossRef]
19. Alturki, T.M.M.; Karaağaç, M.O.; Ergün, A. Performance analysis of a stationary parabolic trough solar collector with a flat metallic receiver incorporating paraffin wax PCM. *Energy Convers. Manag.* **2026**, *356*, 121355. [CrossRef]
20. Lim, C.S.L.; Sobhansarbandi, S. A robust transient modeling approach for an energy storage-based concentrated solar thermal collector. *Renew. Energy* **2026**, *256*, 124360. [CrossRef]
21. Hassan, Y.I.; Gamal, M.; Megalla, K.F. Enhancing overnight operation of solar parabolic trough desalination plants using a multi-chamber PCM-integrated absorber tube: A 3D CFD parametric study. *Desalin. Water Treat.* **2026**, *328*, 101904. [CrossRef]
22. Wasankar, K.S.; Gulhane, N.P. Review of various solar cavity receivers of parabolic dish concentrators with design aspects and heat loss analysis. *J. Therm. Eng.* **2024**, *10*, 756–772. [CrossRef]
23. Nandanwar, Y.N.; Walke, P.V. Performance analysis of phase change material (PCM) integrated conical cavity receiver in solar parabolic dish collector. *Energy Storage Sav.* **2025**, *4*, 166–178. [CrossRef]
24. Saravanan, R.; Karthikeyan, A.; Jayaprabakar, J.; Rajan, T.S.; Vengadesan, E. Energy, exergy, and enviro-economic analysis of a solar receiver with phase change material for a parabolic dish collector. *Environ. Prog. Sustain. Energy* **2025**, *44*, e14613. [CrossRef]
25. AI Abdelaziz, N.; Bouali, B.; Guerraiche, D.; Zaitri, T. Phase change material integration in elliptical double-tube receivers: A novel approach to reduce thermal stress and boost energy storage in parabolic trough collectors. *J. Mech. Sci. Technol.* **2026**, *40*, 2239–2252. [CrossRef]
26. Guclu, T.; Cuce, P.M.; Cuce, E. Experimental 4E analysis (energy-exergy-economic-environmental) of hybrid parabolic trough collector-thermoelectric generator-phase change material cogeneration system. *Energy* **2026**, *349*, 140702. [CrossRef]
27. Cai, R.; Sun, Z.; Yu, H.; Meng, E.; Wang, J.; Dai, M. Review on optimization of phase change parameters in phase change material building envelopes. *J. Build. Eng.* **2021**, *35*, 101979. [CrossRef]
28. Zauner, C.; Hengstberger, F.; Etzel, M.; Lager, D.; Hofmann, R.; Walter, H. Experimental characterization and simulation of a fin-tube latent heat storage using high density polyethylene as PCM. *Appl. Energy* **2016**, *179*, 237–246. [CrossRef]
29. Weingrill, H.M.; Resch-Fauster, K.; Lucyshyn, T.; Zauner, C. High-density polyethylene as phase-change material: Long-term stability and aging. *Polym. Test.* **2019**, *76*, 433–442. [CrossRef]
30. Adıyaman, G.; Çolak, L. Design optimization of a new cavity receiver for a parabolic trough solar collector. *Gazi Univ. J. Sci. Part C Des. Technol.* **2024**, *12*, 451–463. [CrossRef]
31. Hachicha, A.A.; Rodríguez, I.; Capdevila, R.; Oliva, A. Heat transfer analysis and numerical simulation of a parabolic trough solar collector. *Appl. Energy* **2013**, *111*, 581–592. [CrossRef]
32. He, Y.-L.; Xiao, J.; Cheng, Z.-D.; Tao, Y.-B. A MCRT and FVM Coupled Simulation Method for Energy Conversion Process in Parabolic Trough Solar Collector. *Renew. Energy* **2011**, *36*, 976–985. [CrossRef]
33. Moradian, A.; Ameri, M.; Majidi, S. Melting expedition in horizontal triplex tube heat exchangers via radial and combined radial-axial fins. *J. Energy Storage* **2022**, *56*, 106129. [CrossRef]
34. Cheng, Z.D.; He, Y.L.; Cui, F.Q.; Xu, R.J.; Tao, Y.B. Numerical simulation of a parabolic trough solar collector with nonuniform solar flux conditions by coupling FVM and MCRT method. *Sol. Energy* **2012**, *86*, 1770–1784. [CrossRef]
35. Hosseini, M.J.; Rahimi, M.; Bahrampoury, R. Experimental and computational evolution of a shell and tube heat exchanger as a PCM thermal storage system. *Int. Commun. Heat Mass Transf.* **2014**, *50*, 128–136. [CrossRef]

36. Mahdi, J.M.; Nsofor, E.C. Solidification enhancement of PCM in a triplex-tube thermal energy storage system with nanoparticles and fins. *Appl. Energy* **2018**, *211*, 975–986. [CrossRef]
37. Ye, W.-B.; Zhu, D.-S.; Wang, N. Numerical simulation on phase-change thermal storage/release in a plate-fin unit. *Appl. Therm. Eng.* **2011**, *31*, 3871–3884. [CrossRef]
38. Li, X.; Chang, H.; Duan, C.; Zheng, Y.; Shu, S. Thermal performance analysis of a novel linear cavity receiver for parabolic trough solar collectors. *Appl. Energy* **2019**, *237*, 431–439. [CrossRef]
39. Pereira da Cunha, J.M.P.; Eames, P. Thermal energy storage for low and medium temperature applications using phase change materials—A review. *Appl. Energy* **2016**, *177*, 227–238. [CrossRef]
40. Pielichowska, K.; Pielichowski, K. Phase change materials for thermal energy storage. *Prog. Mater. Sci.* **2014**, *65*, 67–123. [CrossRef]
41. Yao, Z.; Yang, C.; Chen, B.; Dai, G.; Chen, Y. Computational fluid dynamics analysis of PCM-based ocean thermal engine with external rib turbulators. *Appl. Therm. Eng.* **2024**, *238*, 122054. [CrossRef]
42. Dudley, V.E.; Kolb, G.J.; Mahoney, A.R.; Mancini, T.R.; Matthews, C.W.; Sloan, M.; Kearney, D. *Test Results: SEGS LS-2 Solar Collector*; SAND94-1884; Sandia National Laboratories: Albuquerque, NM, USA, 1994.
43. Al-Abidi, A.A.; Mat, S.; Sopian, K.; Sulaiman, M.Y.; Mohammad, A.T. Experimental study of PCM melting in triplex tube thermal energy storage for liquid desiccant air conditioning system. *Energy Build.* **2013**, *60*, 270–279. [CrossRef]

Disclaimer/Publisher's Note: The statements, opinions and data contained in all publications are solely those of the individual author(s) and contributor(s) and not of MDPI and/or the editor(s). MDPI and/or the editor(s) disclaim responsibility for any injury to people or property resulting from any ideas, methods, instructions or products referred to in the content.